REPORT DOCUMENTATION PAGE

The public reporting burden for this collection of information is estimated to average 1 hour per response, including the time for reviewing instructions, searching existing data sources, gathering and maintaining the data needed, and completing and reviewing the collection of information. Send comments regarding this burden estimate or any other aspect of this collection of information, including suggestions for reducing the burden, to the Department of Defense, Executive Service Directorate (0704-0188). Respondents should be aware that notwithstanding any other provision of law, no person shall be subject to any penalty for failing to comply with a collection of information if it does not display a currently valid OMB control number.

PLEASE DO NOT RETURN YOUR FORM TO THE ABOVE ORGANIZATION.

1. REPORT DATE (DD-MM-YYYY)	2. REPORT TYPE	3. DATES COVERED (From - To)
25-04-2011	FINAL	15-03-2008 to 31-01-2011

4. TITLE AND SUBTITLE
Ultra High Speed Single Electron Memory Devices based on Carbon Nanotube Quantum Dots

5a. CONTRACT NUMBER
N/A

5b. GRANT NUMBER
FA9550-08-1-0134

5c. PROGRAM ELEMENT NUMBER

6. AUTHOR(S)
Yang, Dr. Eui Hyeok
Strauf, Dr. Stefan

5d. PROJECT NUMBER
FA9550-08-1-0134

5e. TASK NUMBER
N/A

5f. WORK UNIT NUMBER
N/A

7. PERFORMING ORGANIZATION NAME(S) AND ADDRESS(ES)
Dr. Kitt Reinhardt   [Tel: (703) 588-0194; email: kitt.reinhardt@afosr.af.mil]
AF Office of Scientific Research, Room 3112
875 N. Randolph Street, Arlington, VA 22203

8. PERFORMING ORGANIZATION REPORT NUMBER
FA9550-08-1-0134

9. SPONSORING/MONITORING AGENCY NAME(S) AND ADDRESS(ES)
AF Office of Scientific Research
875 N. Randolph Street, Arlington, VA 22203

Office of Naval Research - Boston Regional Office
495 Summer Street, Room 627, Boston, MA 02210-2109

10. SPONSOR/MONITOR'S ACRONYM(S)
AFOSR

11. SPONSOR/MONITOR'S REPORT NUMBER(S)
AFRL-OSR-VA-TR-2012-0864

12. DISTRIBUTION/AVAILABILITY STATEMENT
Distribution A

13. SUPPLEMENTARY NOTES
U.S. Provisional Patent Application Serial No. 61/164,101, filed March 27, 2009, and U.S. Provisional Patent Application Serial No. 61/216,298, filed May 16, 2009.

14. ABSTRACT

  We fabricated a 200 nm quantum dot (QD)-based single electron transistor (SET) device using chemical vapor deposition (CVD) grown in-plane SWNTs. Pronounced conductance oscillation signatures were found in the Coulomb blockade regime demonstrating that the SWNT-QD device operates as a single electron transistor. Further, we observed aperiodic conductivity oscillations in a quasiballistic graphene field effect transistor (GFET), which is of importance for future development of graphene based nanoelectronic devices. In addition, we carried out polarization-resolved -Raman experiments performed at the edges of bilayer graphene flakes, demonstrating that the polarization contrast reflects the fractional composition of armchair and zigzag edges, providing a monitor of edge purity, which is an important parameter for the development of efficient nanoelectronic devices. Finally, to elucidate the role of the localized edge state density, we fabricated dye sensitized antidot superlattices, i.e. nanopatterned graphene. Our investigation provides new insights into the interplay of localized edge states in antidot superlattices and the resulting band bending, which are critical properties to enable novel applications of nanostructured graphene.

15. SUBJECT TERMS
Nanoelectronics, optoelectronics, graphene, carbon nanotube, single electron transistor, field effect transistor, antidot superlattices

16. SECURITY CLASSIFICATION OF:			17. LIMITATION OF ABSTRACT	18. NUMBER OF PAGES	19a. NAME OF RESPONSIBLE PERSON
a. REPORT	b. ABSTRACT	c. THIS PAGE			Dr. Eui Hyeok Yang
U	U	U	SAR		19b. TELEPHONE NUMBER (Include area code) 201-216-5574

AFOSR Final Performance Report

Project Title: **Ultra-High-Speed Single Electron Memory Devices based on Carbon Nanotube Quantum Dots**

Award No.: FA9550-08-1-0134

Start Date: March 13, 2008

Program Manager: Dr. Kitt Reinhardt
Air Force Office of Scientific Research
Arlington, Virginia 22203-1768
TEL: (703) 588-0194. FAX (703) 696-8481.
E-mail: Kitt.Reinhardt@afosr.af.mil.

Principal Investigator: Prof. Eui-Hyeok Yang
Stevens Institute of Technology
Castle Point on the Hudson, Hoboken, NJ 07030
TEL: 201-216-5574, FAX: 201-216-8315
E-mail: **eyang@stevens.edu**

Co-Investigator: Prof. Stefan Strauf
Stevens Institute of Technology
Castle Point on the Hudson, Hoboken, NJ 07030
TEL: 201-216-5639, FAX: 201-216-8315
E-mail: **strauf@stevens.edu**

Co-Investigator: Prof. Frank Fisher
Stevens Institute of Technology
Castle Point on the Hudson, Hoboken, NJ 07030
TEL: 201-216-8913, FAX: 201-216-8315
E-mail: **ffisher@stevens.edu**

Co-Investigator: Prof. Daniel Choi
Chemical & Materials Engineering
University of Idaho, Moscow
TEL: 208-885-0352, FAX: 208-885-0154
E-mail: **dchoi@uidaho.edu**

Accomplishments/New Findings:

- SETs were made by registered in-plane growth utilizing tailored nanoscale catalyst patterns and chemical vapor deposition.

- Metallic SWCNTs were removed by an electrical burn-in technique and the common gate hysteresis was removed using PMMA and baking, leading to field effect transistors with large on/off ratios up to 10^5.

- Further segmentation into 200 nm short semiconducting SWCNT devices created quantum dots which display conductance oscillations in the Coulomb blockade regime.

- The demonstraton of registered in-plane growth opens possibilities to create novel SET device geometries which are more complex, i.e. laterally ordered and scalable, as required for advanced quantum electronic devices.

- Conductivity oscillations were observed with aperiodic spacing to only one side of the tunneling current in a dual-gated graphene field effect transistor with an n-p-n type potential barrier. This observation is of importance for future development and modeling of graphene based nanoelectronic devices.

- Raman spectroscopy was used to monitor the composition of graphene's zigzag/armchair edges. The polarization contrast reflects the fractional composition of armchair and zigzag edges, providing a monitor of edge purity, which is an important parameter for the development of efficient nanoelectronic devices.

- To elucidate the role of the localized edge state density, we fabricated dye sensitized antidot superlattices, i.e. nanopatterned graphene. The fluorescence from deposited dye molecules was found to quench strongly as a function of increasing antidot filling fraction, whereas it was enhanced in unpatterned but electrically back-gated samples.

- Our study provides new insights into the interplay of localized edge states in antidot superlattices and the resulting band bending, which are critical properties to enable novel applications of nanostructured graphene for light harvesting and photovoltaic devices.

Summary

The major objective of this project is to investigate carbon-based transistor devices for nanoelectronics and optoelectronics. **Firstly**, we developed a registered chemical vapor deposition (CVD) growth method to form in-plane SWCNTs between predefined nanoscale catalyst patterns. We furthermore developed a technique to purify the SWCNT chirality after growth by eliminating metallic tubes and preserving semiconducting tubes, leading to SWCNT field-effect transistors with current on/off ratios up to 10^5. These devices were than transformed into quantum dot (QD)-based single electron transistor (SET) devices by reducing the contact spacing. Pronounced conductance oscillation signatures were found in the Coulomb blockade regime demonstrating that the SWCNT-QD device operates as an SET up to temperatures of about 200 K. **Secondly**, we fabricated and characterized dual-gated graphene field effect transistors (GFET) as an alternative approach. In particular, we investigated a quasiballistic GFET with an additional n-p-n type potential barrier and observed aperiodic conductivity oscillations to only one side of the tunneling current. The spacing and width of these oscillations were found to be inconsistent with pure Fabry–Perot-type interferences fringes of electron waves, but are in quantitative agreement with theoretical predictions that attribute them to resonant tunneling through quasibound impurity states within the barrier. This observation may be understood as a novel signature of Klein tunneling in graphene heterojunctions and is of importance for future development and modeling of graphene based nanoelectronic devices. **Thirdly**, we carried out polarization-resolved μ-Raman experiments performed at the edges of bilayer graphene flakes. We found a strong dependence of the intensity of the G band on the incident laser polarization, with its intensity dependence being 90° out of phase for the armchair and zigzag case, in accordance with theoretical predictions. For the case of mixed-state edges we demonstrate that the polarization contrast reflects the fractional composition of armchair and zigzag edges, providing a monitor of edge purity, which is an important parameter for the development of efficient nanoelectronic devices. **Finally**, to elucidate the role of the localized edge state density, we fabricated dye sensitized antidot superlattices, i.e. nanopatterned graphene. The fluorescence from deposited dye molecules was found to quench strongly as a function of increasing antidot filling fraction, whereas it was enhanced in unpatterned but electrically back-gated samples. This contrasting behavior is strongly indicative of a built-in lateral electric field of up to 260 mV accounting for p-type doping as well as fluorescence quenching due to dissociation of electron-hole pairs from attached dye molecules. Our investigation provides new insights into the interplay of localized edge states in antidot superlattices and the resulting band bending, which are critical properties to enable novel applications of nanostructured graphene for light harvesting and photovoltaic devices.

1. Research Objectives

The major objective of this project is to investigate carbon-based nanostructures for nanoelectronics and optoelectronics. The in-plane semiconducting SWNT structures directly grown from catalyst patterns were studied for their quantized electron energy properties (**Figure 1**). The initial research plans are: 1) Synthesize SWNTs aligned with patterned catalyst tips; 2) Create semiconducting SWNT-based QDs; and 3) Study quantized electron energy properties of SETs. Additional experiments were performed on graphene FET devices and antidote structures.
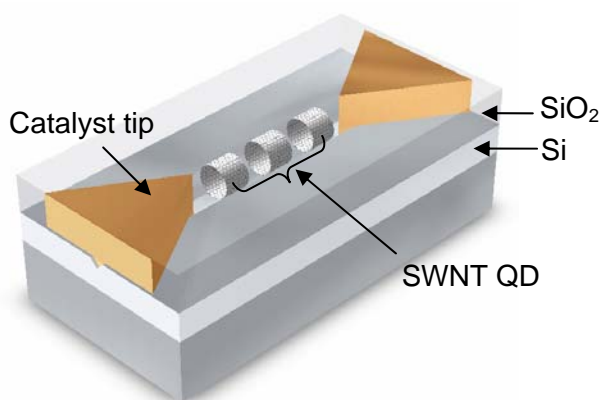

Figure 1. Conceptual schematic of the proposed SWNT-QD device.

2. Technical Results

2.1. CVD growth of CNTs

We have developed a chemical synthesis method of metal oxide nanoparticles, and a site-specific patterning of catalyst dots using a nanoimprinting technique. The patterns were defined in part by an etch mask in the form of a high quality aluminum (Al) film. A gas mixture for reactive ion etching (RIE) was composed of pure chlorine to argon in the ratio of 1:0.2 while using 300-400 Watts. The RIE power with 600 Watts Induction Coupling Plasma (ICP) power was found to be an optimum condition for fused silica material. The addition of argon gas to C_4F_8 was found to contribute to the anisotropic etching, and resulted in vertical sidewall profiles inevitable for an effective lift-off process. Following the plasma enhanced formation of silicon oxide and fluorine ions, volatile products of Si-fluorides were formed and driven away at elevated temperature. $Fe(CO_3)_5$ in octyl ether and oleic acid for 2 hour at $140^{o}C$ followed by reflux for 1 hour at $350^{o}C$. The Fe nanoparticles were oxidized by adding trimethyl amine N-oxide and heating at $140^{o}C$ followed by reflux for 1 hour. The resulting Fe-oxide nanoparticles were precipitated using ethanol. CNTs tend to grow perpendicular to the local substrate surface if the catalyst material is damaged by heat during the CNT growth. This indicates capping a catalyst layer is necessary to

3

grow CNTs laterally across a patterned trench. After we made experiments with various thicknesses of high-melting point metallic thin films, about 20 nm thick niobium (Nb) layer deposited in catalyst material was found to avoid vertical growth of CNTs. Optimized growth process enabled growth of SWNTs using low-pressure CVD with a methane-hydrogen mixture (CH_4:H_2 = 8:1), pressures of 5-8 torr, and typical growth temperatures of 750-800°C.

2.2 Segmentation of SWNTs

We have created CNT sections down to 58 nm feature sizes, and are in the process of varying patterning parameters to find the optimal patterning conditions to create <20 nm features. Oxidation parameters that were varied were voltage, tip-substrate distance (setpoint), and tip speed (or holdtime per pixel) under high (>60%) and low (40%) relative humidity conditions. The dependent parameter was feature size (depth and width) of the oxidized sample. In the oxidation experiments, voltage was varied from -2 to -10V, setpoint from 20 to 160 nm, and tip speed from .1 to 1.7 μm/s. Decreasing absolute voltage oxidizes a smaller number of carbon atoms such that less carbon material is removed per pixel. Increasing setpoint requires that the tip move vertically further away from the CNT thereby stretching the condensed water meniscus and reducing its x-y dimensions, again removing less carbon material per pixel. With decreased hold time (or increased speed), the tip spends less time oxidizing per pixel, creating smaller features. Finally, decreasing humidity before a threshold of 20% simply means the water meniscus grows smaller and smaller which again implies reduced oxidation area. **Figure 2** shows schematic diagram of AFM oxidation lithography setup. An external voltage source is used to ground the CNT and negatively bias the AFM tip. **Figure 3** depicts feature-width dependence of (a) CNT and (b) few layer graphene on AFM tip speed.
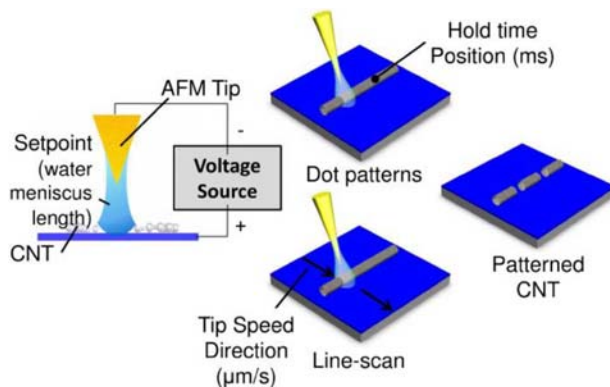

Figure 2. Schematic diagram of AFM oxidation lithography setup. An external voltage source is used to ground the CNT and negatively bias the AFM tip. The water meniscus, which naturally condenses around the tip, and CNT facilitates local oxidation of the CNT upon application of the electric field. The figures on the right illustrate the difference between dot patterns and line scans during oxidation. Dot patterns (top) involve holding the tip stationary at a point above the CNT (hold time position) and applying voltage to fabricate the patterns, while line scans (bottom) involve scanning the tip perpendicularly across the CNT at a constant tip speed and applying continuous voltage.
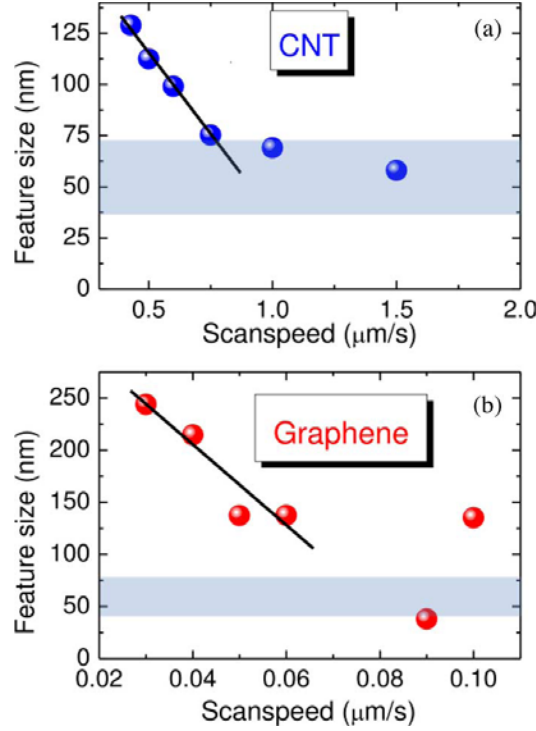
Figure 3. Feature-width dependence of (a) CNT and (b) few layer graphene on AFM tip speed. In (a), as tip speed decreases and thus hold time per pixel increases, more carbon material is oxidized. Smaller feature sizes can be achieved for relatively fast tip speeds (1.00–1.50 μm/s) corresponding to short hold times. This trend is seen in (b) for slower tip speeds (0.03–0.06 μm/s) corresponding to longer hold times, but the feature-size dependence becomes inconsistent approaching faster tip speeds (above 0.06 μm/s.) This behavior is attributed to the hydrophobicity of graphene, especially under low humidity conditions.

Our initial plan was to create QDs using AFM-based local anodic oxidation. While we plan to reduce feature size by further finding the optimal range of voltage, holdtime, setpoint and humidity, we learned that it is extremely difficult and inefficient to create QDs using this method. Therefore, in the future the QDs will be created using top-gated SWNTs to electrostatically confine electrons using 10nm wide top gates. As a pathfinder approach, in this work, we created a short CNT-QD device by reducing the contact spacing from 2000 nm to 200 nm: As is well known, SWNTs with any type of chirality being either metallic or semiconducting or even multiwall CNTs can operate as an SET if the device temperature is low enough, i.e. lower than the quantized level spacing and the charging energy. For CNTs which are several microns long between the source-drain contacts the SET effect can only be observed at milli Kelvin temperature due to the small confinement energies of the CNT. In effect the Schottky barriers at the contacts define the quantization along the wire direction. We identified a semiconducting SWCNT bridging the 2 micron gap between contacts and added extra electrodes as shown in **Figure 4**. These electrodes effectively shorten the segment length by one order of magnitude down to 200 nm. The larger confinement energy allows SET measurements at 5K.
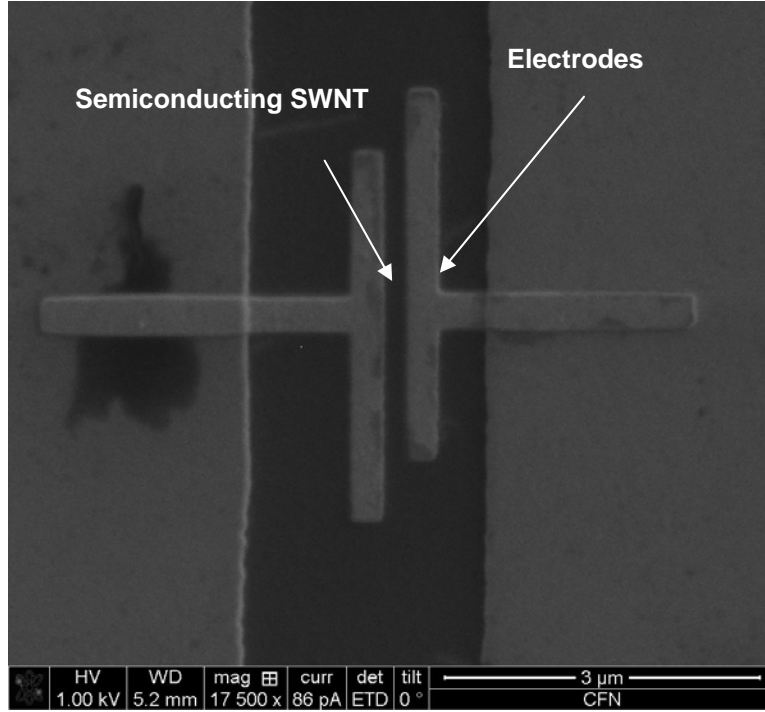
5

Figure 4: Fabricated preliminary SET structure with a 200 nm SWNT segment acting as a quantum dot. The added smaller electrodes effectively reduce the CNT segment length from the 2 μm as grown over the electrode gap down to 200 nm.

2.3 Experimental techniques: In order to characterize electron transport properties in nanoelectronic devices made from CNTs and graphene we have developed two methods to analyze the transconductance behavior. The first technique measures directly the source-drain current I_{sd} as a function gate voltage V_g and the second technique measures the differential conductance dI/dV as a function of source-drain voltage V_{sd} and gate voltage.

The direct current measurements were performed with two Keithley 2400 SourceMeters interfaced with LabView. The technique is however limited by the minimum current resolution of 50 pA and thus not suitable to fully resolve the on-off ratio of FETs or single electron transport signatures. To further improve the technique we have recently used a current meter with higher sensitivity and integrated it with a home-built electronic circuit and pre-amplifier into the setup. This system achieved a sensitivity down to about 800 fA which is sufficient to resolve single electron charging in the coulomb blockade regime.

The second technique utilizes a two-wire probe technique to directly determine the conductance dI/dV of the device under test as a function of V_{sd} and V_g. Since the resistance of the device in the Coulomb blockade regime is sufficiently large compared to the contact resistance the differential technique can be implemented by modulating the source-drain voltage at a fixed frequency (13Hz) and probing the resulting alternating source-drain current with a lock-in amplifier. We used a Stanford Research Systems SR830 lock-in Amplifier and constructed a voltage divider circuit which adds the DC and the AC stimulous as shown schematically in **Figure 5.** The lock-in was interfaced with LabView and the voltage sources for V_{sd} and V_g. The adder circuit acts as a 1000:1 voltage divider for the ac signal and a 100:1 divider for the dc signal. The composite AC+DC signal was applied to the source side of the device. The drain was fed back into the lock-in for the current dI measurement. The gate was biased by another Keithley 2400 with respect to the common ground.
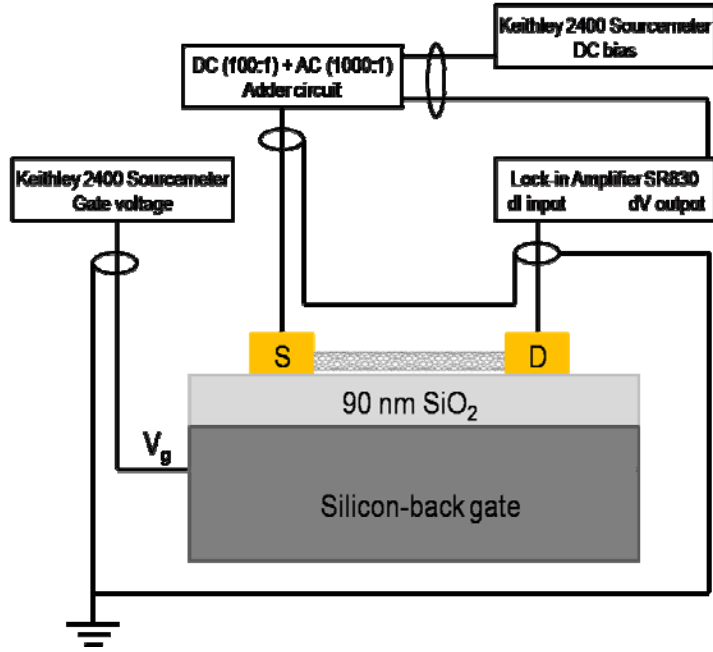

Figure 5: Schematic of the developed two-wire lock-in technique. The AC signal from the lock-in was divided down and combined with a DC stimulus from a programmable voltage source and the resulting AC current was detected with a lock-in amplifier.

To carry out low-temperature measurements in a cryostat the device bond pads were connected to the chip carrier bond pads using 25 μm Au wires. We found that it is essential to have a good grounding scheme for both, the wire bonding process and the cryostat loading procedure (electrostatic discharge). If the wire bonder is operated in the standard mode where it applies an ultrasonic stimulus to the bond-tip the resulting current can destroy the nanostructures. We thus modified the system to bond with heat (~100° C) and force only while grounding the bond-tip. This technique worked successful when utilizing 200 nm thick Cr/Au metallization for the CNT bond pads.

2.4 Transformation of CNT arrays into FET devices with high on-off ratios: CNTs display either metallic or semiconducting properties corresponding to their chirality, which cannot be perfectly controlled in the CVD growth process. We have previously reported a detailed study of the transport characteristics of the CNT-FETs as a function of the number of CNTs bridging the

7

contact gap [1]. Devices containing more than 10 CNTs usually display CNT-FET on/off ratios of less than 2. Better results have been achieved for smaller devices containing only 3 CNTs displaying on/off ratios up to 370 at room temperature. Such relatively low on/off ratio exists because CNT arrays contain both metallic and semiconducting CNTs. Metallic CNTs give rise to a non-vanishing off-state current, which masks the high on/off ratio of the semiconducting CNTs. Since the metallic CNTs cannot be fully avoided in the CVD growth we have developed a technique to controllably break metallic CNTs on large arrays without affecting the semiconducting ones**.** Since the metallic tubes in mixed arrays are detrimental for the device performance, an improvement FET performance is expected. **Figure 6 (a)** shows a plot of the source-drain current I_{sd} versus source-drain voltage V_{sd} sweeps. The back gate was held constant at V_g= +20 V to switch the p-type semiconducting CNTs into their off-state. This prevents current flow through semiconducting CNTs and protects them from burning in the electrical breakdown procedure.
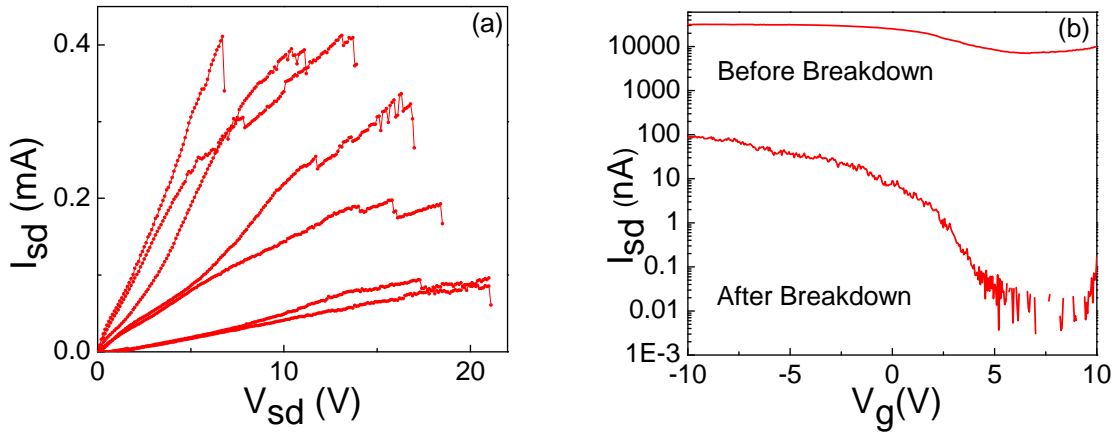

Figure 6: (a) Plot of source-drain current I_{sd} versus source-drain voltage V_{sd} for the whole breakdown procedure. (b) Characteristic of source-drain current I_{sd} versus gate voltage V_g before and after breakdown procedure. The on-state current was decreased due to the elimination less conducting channel, but the on/off ratio was improved up to 10^4.

Several breakdown events are visible at higher voltages. In order to eliminate all the metallic CNTs, we increased V_{sd} until the first metallic CNT broke. The whole breakdown procedure was monitored by plotting the real-time current value. Once the current starts to fall, we stopped increasing V_{sd} to prevent further damage. The next breakdown attempt starts from zero bias voltage until another metallic CNT breaks. After each breakdown, a characteristic I_{sd} versus V_g sweep was performed to examine the on/off ratio improvement**. Figure 6 (b)** shows the result after the first and last break-in event, while steps in between are not shown. The initial I_{sd} versus V_g curve in **Figure 6 (b)** recorded at 100 mV V_{sd} shows a rather small on/off ratio of about 2.

When all metallic CNTs were removed, the field effect behavior of the device is dramatically enhanced and FET on/off ratio improved in the best case by 5 orders of magnitude to about to 10^5. We have therefore successfully transformed mixed CNT arrays into pure arrays of semiconducting SWNTs with high on/off ratios.

2.5. Control of conductance hysteresis in CNT FETs: The semiconducting SWNT FETs created by the technique described in **Section 2.2** have outstanding electrical properties. While it is possible to create only one SWNT between an electrode pair by further reducing the electrode size, we have initially investigated arrays with larger electrodes with typically 10-20 SWNTs grown over the 2 micron contact spacing. Therefore, several semiconducting SWNTs contribute after burn-in to the total current in the on-state which reaches 0.1 μA under 100 mV source-drain voltage. The on-state current varies linearly with the source-drain voltage and highest on-state currents of about 1 μA have been achieved at about 1V bias voltage (not shown), corresponding to on/off ratios approaching 10^5. These values are among the highest reported for CNT FETs which are back gated. Further improvement can only be achieved by top gating with thin high-k dielectrics. Despite these outstanding transport properties, our fabricated devices suffer from gate hysteresis. The gate hysteresis causes the transconductance characteristics of the CNT-FETs to be strongly affected by the sweep direction of the gate voltage, i.e. sweeping from negative to positive voltages or sweeping backwards results in different characteristics**.**

The hysteresis effects do not only depend on the V_g sweep direction, but they also depend on the chosen sweep range and sweep time. The larger the sweep range the larger the hysteresis effect (data not shown here). As is well known, the hysteresis is caused by charge trapping within the local CNT environment and is absent on elevated CNTs bridging an air gap. In particular, it is not only affected by moisture in ambient conditions but also by the SiO_2 surface-bound water attached to the silane groups proximal to the nanotubes [6]. **Figure 7 (a)** shows the hysteresis sweep of an uncapped device measured in ambient atmosphere under a *gate* sweep range from - 10 V to + 10 V. As can be seen, the threshold voltage for the on/off FET effect switching changes by more than 8V. This hysteresis makes it nearly impossible to operate the FET as a SET device.
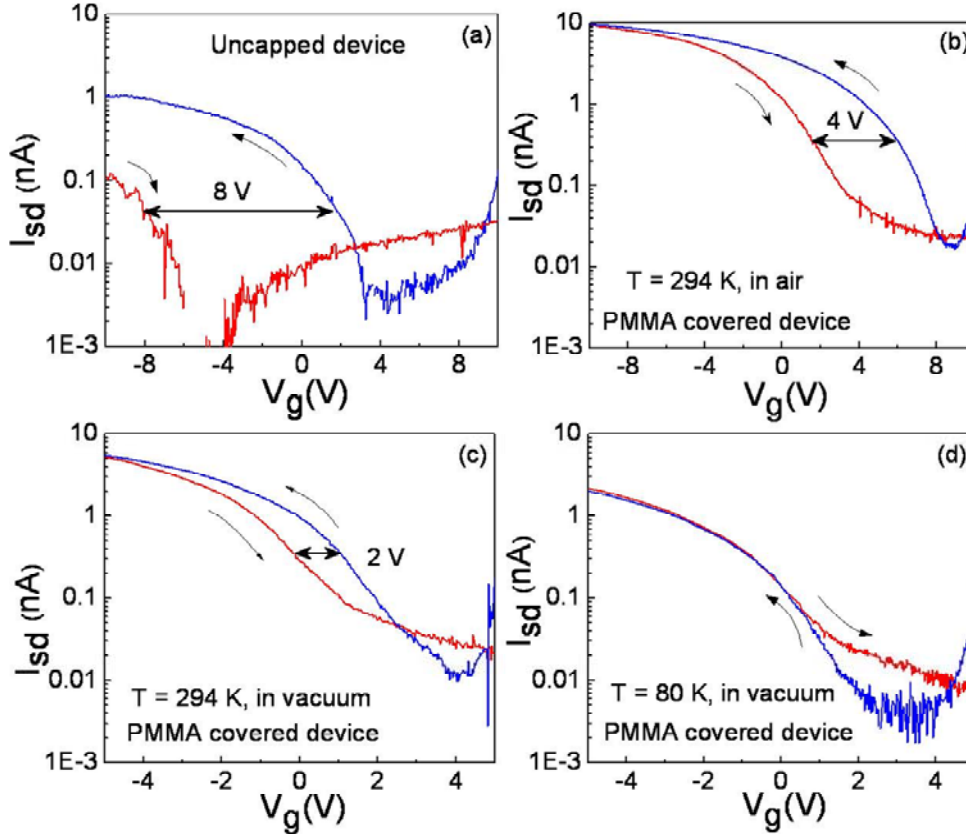
Figure 7: Characterization of gate hysteresis. (a) I_{sd} versus V_g in forward and backward sweep direction on the uncapped device. Same sweep for a PMMA coated device held in air at RT (b), under vacuum at RT (c), and at liquid nitrogen temperatures (d). All data are recorded with 100 mV source-drain bias.

In order to eliminate hysteresis we developed a procedure following the work by Kim *et al*. [2]. Samples have been capped by PMMA followed by baking on a hot plate at 150 °C for several days in ambient air to remove surface-bound water molecules. The PMMA furthermore effectively encapsulates the CNT from the environment making measurements reproducible **Figure 7 (b)** shows a gate sweep of the same device capped by PMMA and baked out while held in air. The magnitude of hysteresis was reduced to about 4 V and the current in the on-state was identical. **Figure 7 (c)** demonstrates a further reduction of that gate hysteresis if the device is wire bonded and measured in vacuum, were the voltage shift was further reduces to about 2V. We also observed that the sample is less affected by the sweep range. Even though the nanotube was covered by PMMA, measurements show that vacuum environment can further reduce the hysteresis effect, indicating that the PMMA layer acts as a permeable membrane. After cooling the device to 80 K we observed a near-zero hysteresis effect in the same device as shown in **Figure 7 (d)**. Since residual mobile charges are frozen out at low temperature the local CNT environment is less affected by changing the applied gate voltage direction. In conclusion, the hysteresis was strongly reduced utilizing the PMMA coating and baking technique and by

cooling the device down to liquid nitrogen temperatures. This successful reduction in hysteresis has finally allowed us to measure SET behavior in our CVD grown CNT-QD devices.

2.6. Electrical characterization of CNT-FET devices operating as SET up to 200 K: As described in **Section 2.2**, we have fabricated a QD device by reducing the contact spacing from 2000 nm to 200 nm. The as-grown array containing about 20 CNTs was first burned-in to obtain pure semiconducting SWNTs arrays and the gate hysteresis effect was removed using the PMMA coating technique. After that one particular semiconducting SWNT was identified in SEM and its contact spacing was reduced to 200 nm. While we still measure on a device with about 20 semiconducting SWNTs across, the transport signatures are expected to be dominated by the SET behavior of the shortened SWNT and the remaining 2 micron long semiconducting SWNTs are silent in their off state.

Figure 8 shows the SET conductance oscillation signatures recorded at 5.2K base temperature of the liquid Helium flow cryostat. As shown in **Figure 8 (a)**, electron transport over the discrete QD states, which are spaced out by ΔE, can be controlled by changing the transport window width (E_{FS}-E_{FD}), which is defined by the difference in Fermi levels between source and drain. The larger this energy difference, which scales linearly with V_{SD}, the larger the number of transport channels contributing to the observed current. In addition, with each additional electron located on the QD the electrostatic potential energy U_0 increases, which affects the single electron transport. Therefore, the conduction oscillations vanish with increasing source-drain voltage as shown in **Figure 8 (b).** This is in agreement with the expected closing of the Coulomb diamonds typically observed when plotting the conductance as a function of source-drain voltage and gate-voltage. The role of the gate voltage is to tune the QD DOS through the transport window defined by the source-drain voltage. As a result, conductance oscillations are observed in **Figure 8 (b-d).** For the larger transport of 1.5 mV highlighted in **Figure 8 (c)** the discrete electron jumps appear more as a step function since the transport window is broad enough to allow several transport channels to contribute simultaneously. Thus, the current does not go down in between each step. At the smaller transport window highlighted in **Figure 8 (d)** the conductance oscillations appear more like discrete peaks, since the window is small enough that only individual energy levels contribute to the total current. It is observed that the overall spacing of the Coulomb blockade peaks is not constant at fixed V_{SD} but slightly anharmonic. This effect can have several reasons: First, there is still a residual hysteresis since this device was only annealed for 12 hrs. Thus the frozen charges can affect the harmonicity of the energy level spacing. Second, the particular device contains other 2 micron long semiconducting CNTs which can contribute to the total current. And third, the 200 nn long segment is still long enough to allow formation of several QDs along the segment during the carrier freeze out which have a nonlinear interplay and level spacing.
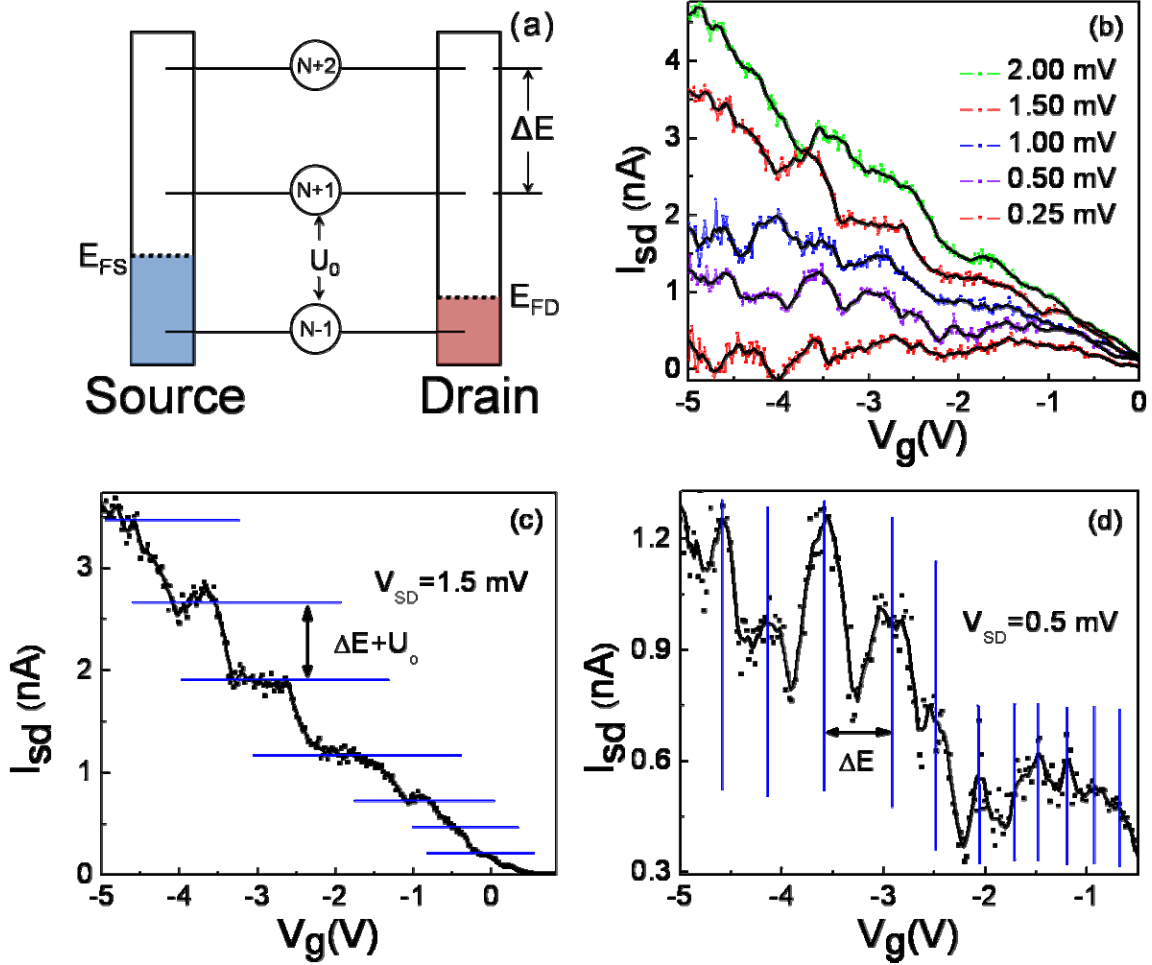
Figure 8: Characterization of SET performance. (a) Energy diagram for Coulomb blockade illustrating the transport window (E_{FS}-E_{FD}), the QD energy spacing ΔE and potential energy U_0 which increases for each additional loaded electron. (b) .I_{sd} versus V_g sweeps showing Coulomb oscillations which vanish at higher V_{sd} bias. (b). Panels (c) and (d) highlight two traces taken at V_{sd} = 1.5 mV (c) and V_{sd} = 0.5 mV (d). All measurements are carried out at 5.2K.

In addition, **Figure 9** shows a temperatures dependent study of the Coulomb oscillation sin the SER device. Pronounced peaks related to single electron effects are visible up to temperatures of about 200 K. At higher temperatures the thermal energy is larger than the combined values of charging energy and quantum dot level spacing such that the signatures start to disappear.
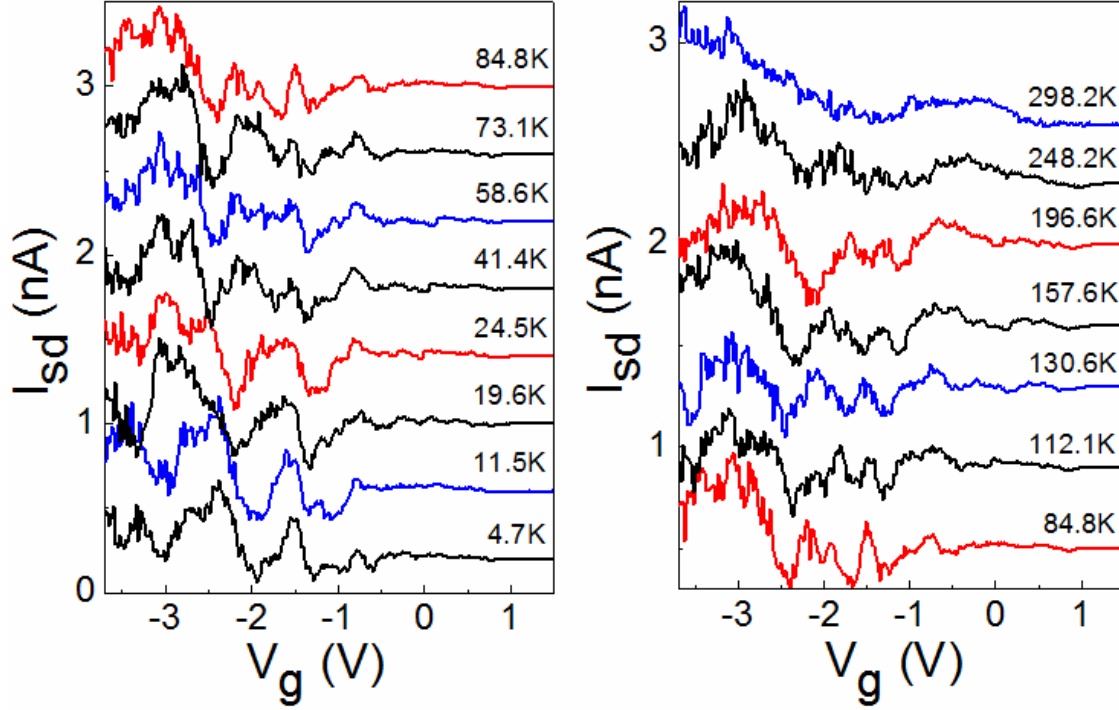
Figure 9: Dependence of Coulomb blockade oscillations on temperature recorded at a source-darin voltage of 0.5 meV. Pronounced single electron signatures are visible up to about 200 K.

2.7. Graphene FET

Graphene is a novel material related to carbon nanotubes displaying similar electronic properties such as ballistic transport, high mobility, and a field effect. The 2D character of monolayer graphene makes combined with the possibility to fabricate nanostructures of arbitrary shapes in large quantity at predefined positions using electron beam lithography makes graphene a promising alternative to CNT-based nanoelectronic devices. We have thus explored possibilities to realize nanostructures with similar functionality as compared to the CNT-FETs and CNT-SETs described above with the goal to overcome the problem of scalability and chirality inherent to carbon nanotues.

In particular, we explored nanofabricated graphene-based double-gated FETs in order to study ballistic transport and electron phase coherence to realize novel sensors based on electron wave interference effects. As a result towards the exploitation of the proposed graphene memory concept, we have successfully fabricated and characterized a ballistic Klein transistor (**Figures 10 and 11**). In this device, the top-gate was electrically isolated from the graphene layer by a 10nm Al_2O_3 gate oxide. Independent biasing of the local top-gate with respect to the back-gate created the desired *n-p-n* regions, by way of electrostatic confinement, which defines an FET within the graphene layer as illustrated in **Figure 11 (a)**. The global back-gate of the device was

13

used to position the Fermi level in the entire device at the Dirac point, while the local top gate was used to induce a potential barrier, thereby creating the n-p-n regions in the device.

The measured I-V_{TG} characteristic of the device in **Figure 11 (a)** shows evidence of chiral Klein tunneling – an increase in tunnel current through the local potential barrier with increasing barrier height past a minimum point, a process that is only possible in the ballistic transport regime. The seemingly

Figure 10: High-resolution optical microscope images of a fabricated double-gated graphene FET. Two source and two drain contacts have been made to allow four-point probing. The fifth contact in the middle forms a top-gate separated by a 10 nm Al_2O_3 gate oxide. The size of the graphene flake is about 2x10μm. [3]

paradoxical increase in the tunneling current as a function of an increasing energy of the electrostatic barrier can be understood in terms of chiral tunneling across the barrier. Furthermore, the minimum of the source-drain current decreases the closer the back gate voltage is to the charge neutrality condition in the *n* region, as indicated by the dotted line in **Figure 11 (a)**. The observation of Klein tunneling in these structures is useful in ascertaining the ballistic mean free path. One can infer from the data that the ballistic mean free path is larger or equal to 100 nm, which is the tunnel length as defined by the top-gate length; modeling efforts are underway to better understand the device performance.
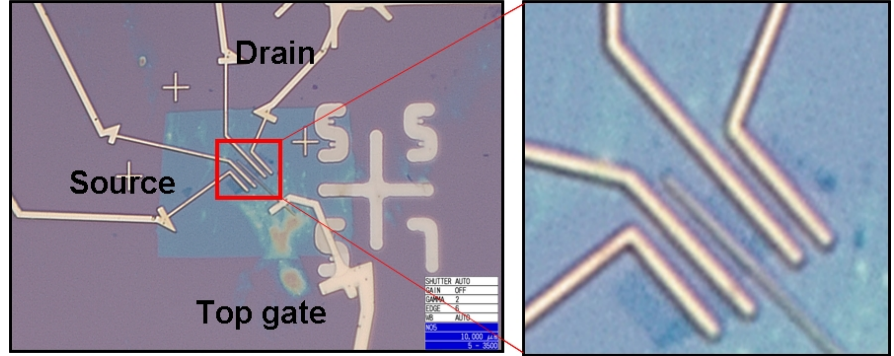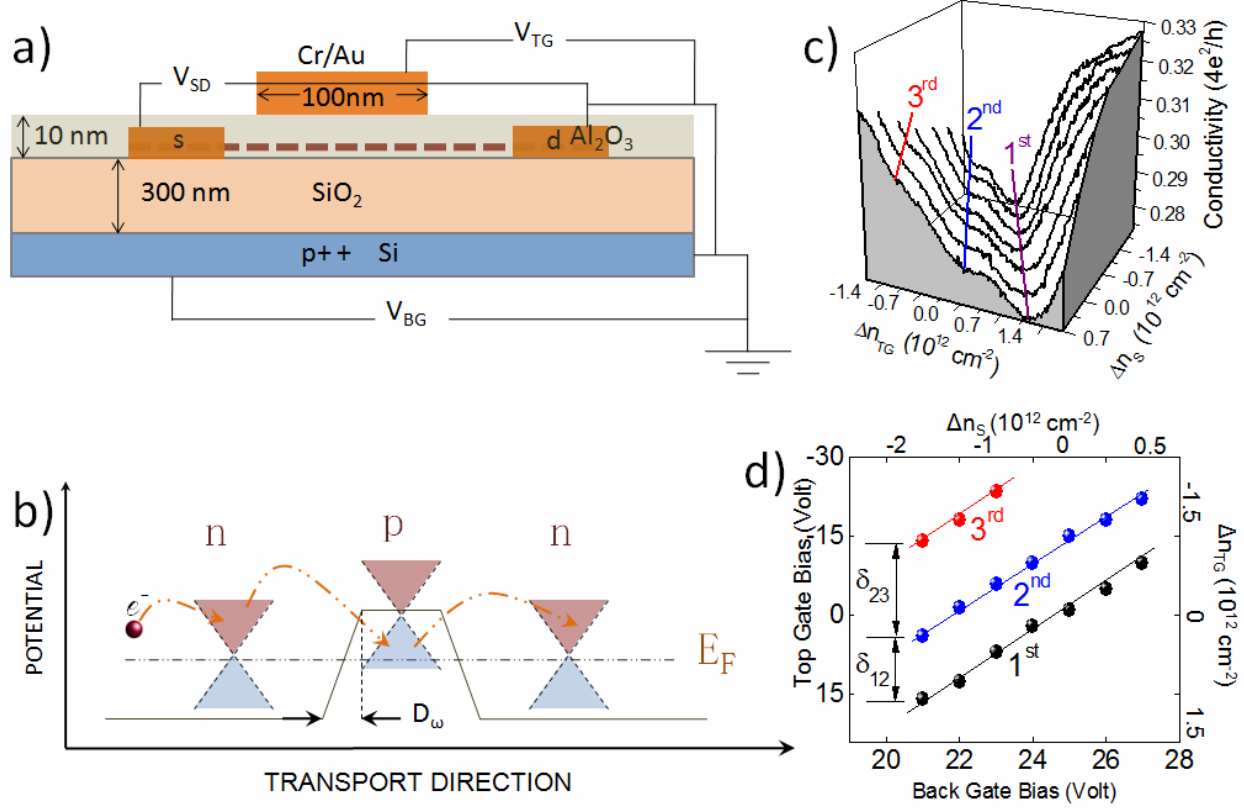
Figure 11: a) Schematic of the device and biasing scheme, which gives rise to the electrostatic barrier configuration as shown in b). Characteristic asymmetrical conductance oscillations on only one side of the tunneling current are observed as a function of top gate bias c) and are indicative of Klein tunneling. A further indication and differentiation from Fabry-Perot oscillations are the magnitude and spacing of the peaks as shown in d).

2.8. Atomically Precise Etching of Graphene

Narrow GNRs have a bandgap inversely proportional to the width of the GNR. Here, a key fabrication challenge for GNR devices is the reduction of edge disorder (formation of a mixture of zigzag and armchair edges and widths that vary along the ribbon length) [4]. Recently, the PIs have successfully demonstrated atomically precise cutting of graphene patterns to create GNRs with specific boundaries (**Figure 12**). The preferential nanomachining technique will enable the atomically precise, directional cutting of graphene layers. Therefore, in addition to pursuing the conventional EBL process to pattern GNR structures, we have developed an alternative, chemical vapor deposition (CVD)-based nanocutting process [5, 6]. When a metal nanoparticle is formed at an edge of graphene at high temperature, a hydrogenation process is initiated to move the particle along the directions of symmetric axes (zigzag or armchair) via a "minimum energy"

path. Hydrogen atoms are absorbed on the surface of the metallic particle, and combined with the carbon atom eject from the graphene surface, leading to atomically precise cutting.

2.9. *Edge State Determination and Monitoring Edge Chirality with Raman Spectroscopy*

An important requirement to maximize the achievable strain tuning effect is that the edge states of the GNR must be predominantly

Figure 12: Recent results by the PI group on atomically precision etching of graphene [4]

of armchair-type since the strain-induced formation of a bandgap is a much smaller effect in the zigzag type edges as compared to armchair edges [7]. To this end, the characterization of the degree of the edge state purity created in the fabrication process is critical. The PIs have recently demonstrated a novel technique based on Raman spectroscopy which is capable of providing the fractional degree of the edge composition [8]. To this end we have first identified the number of graphene layers in exfoliated flakes using the Raman shift of the G'-band. Since the G'-band is a result of multi-phonon scattering, the resultant spectrum is a convolution of several phonon modes. The anisotropic shift of the constituent phonon modes results in a deviation from the Lorentzian line shape, which changes as a function of the number of graphitic layers, as shown in **Figure 13**.
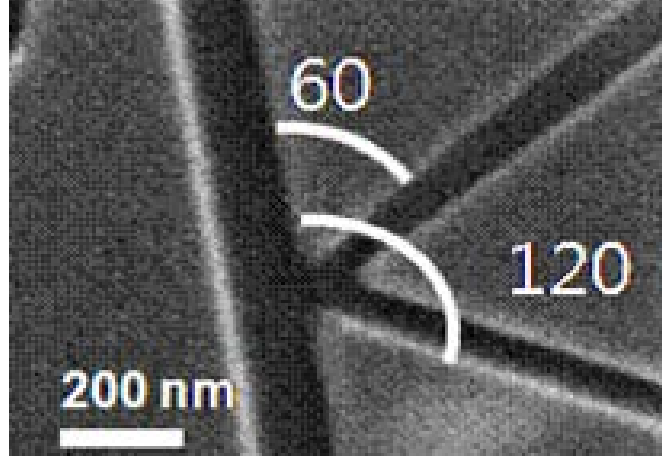
In order to investigate the correlation between graphene's edge chirality and the corresponding Raman signatures, graphene flakes were mechanically exfoliated from natural graphite and deposited onto pre-patterned p+ silicon wafer with a thermally grown 300 nm silicon oxide. Room temperature Raman spectra were obtained using a 2.33 eV laser diode focused down to about 2 μm spot size. Half wave plates were used to rotate the plane of polarization with respect to the sample in the laser excitation path and to rotate the plane of polarization in the collection path back to its original configuration in order to eliminate any errors introduced by the dependence of the spectrometer's grating and other optical components on the polarization of light. There are four prominent spectral bands of graphene in the wavelength range from 1300-2700 cm^{-1}. Each band can be used as a tool to probe different material characteristics. The G' band around 2700 cm^{-1} (sometimes referred to as the 2D band) provides unambiguous

information about the number of constituent graphene layers [9,10]. This phonon band originates from inter-valley scattering of two in-plane transverse optical (iTO) phonons at the K and K' points at the edges of the Brillouin zone [11,12]. The impact of the number of layers on the G' band is shown in Figure 1a. In single-layer graphene, the G' band can be approximated by a single Lorentzian function (**Figure. 14a,** lower panel), whereas several Lorentzian functions are required in the case of multilayer graphene (**Figure 14a**, middle and upper panels), reflecting the splitting of the electronic bands and phonon branches [13]. After peak deconvolution we found that the difference in frequencies of the two dominant subcomponents of the G' band increases with the number of graphitic layers, with values comparable to the ones reported in the literature [19]. Our investigation focuses on exfoliated flakes which have been identified as bilayer graphene.
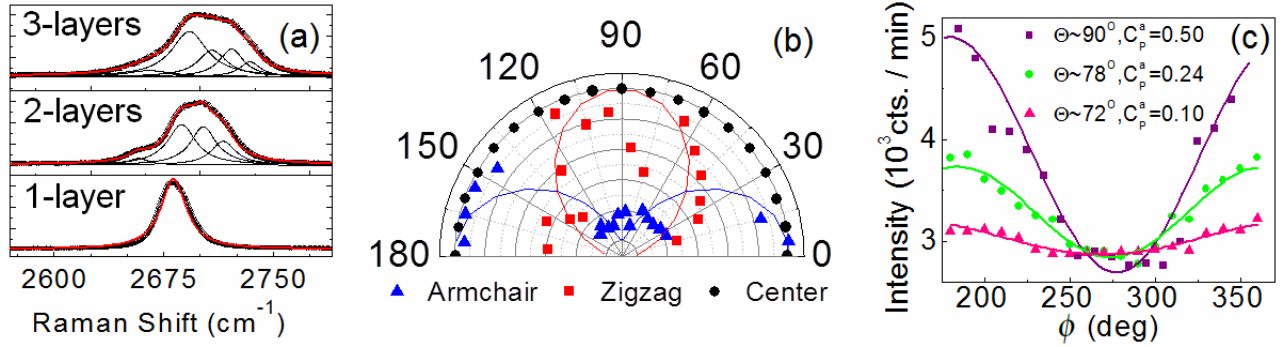

Figure 14 a) Raman spectrum of the G' band taken from a monolayer (bottom), bilayer (middle), and trilayer graphene flake. b) Polarization dependence of the G band recorded from the interior points of monolayer graphene (black dots), from a predominantly armchair edge (blue triangles), and a predominantly zigzag edge (red squares). c) Polarization dependence of the G band for three different armchair edges. All data are recorded at room temperature using an excitation wavelength of 532 nm.

While the G' band is useful in layer metrology analysis, the D and D' bands can be used for edge chirality determination. Raman spectra of different edges of bilayer flakes were recorded under the same polarization conditions and selected from a single large area flake. One particular edge was identified as being zigzag using D / D' band spectroscopy (see discussion below) and used as a reference for measuring all subsequent edge angles. Interestingly, several of the edges possess pronounced D (1350 cm^{-1}) and D' (1620 cm^{-1}) bands, while others lack both bands. The D band originates from inter-valley scattering that connects two adjacent K & K' points at the Brillouin zone boundary via a second order process that requires one iTO phonon and a symmetry

breaking perturbation such as an armchair edge for its activation [14]. Similarly, the D' band is a weak intra-valley transition that requires one iLO phonon and a symmetry break. The presence (absence) of these bands has been shown to correspond to armchair (zigzag) chiralities in both single layer graphene as well as HOPG. Based on the fact that the chirality of a given edge changes in multiples of 30º, odd multiples correspond to edges with opposite chirality and even multiples correspond to edges with the same chirality. Other edges can be identified as either predominantly zigzag or armchair depending if the angle they make with respect to the edge is closer to an even or an odd multiple of 30º. Thus the angle metrology and the correlation with the presence or absence of the D-band allows us to make a distinction between armchair and zigzag edges. However, the D band does not provide unambiguous information about edge purity since it does not change its oscillator strength accordingly and was found not to exhibit strong polarization dependence.

In contrast to the D band, we found that the G band around 1580 cm^{-1} does provide information about the fractional edge composition. The G band arises from a doubly degenerate intra-valley process that originates from scattering of an iTO phonon or an iLO phonon at the center of the Brillouin zone. For pure zigzag edges, the intensity of the G band is expected to be maximum for an excitation beam polarization that is perpendicular to the edge. Conversely, for armchair edges its intensity maximizes for the incident excitation beam polarization that is parallel to the edge. This phenomenon is still present for mixed edges, however, the degree of the polarization contrast is diminished and is proportional to the amount of mixing of zigzag and armchair boundaries. Purely random edges, i.e. edges comprised of equal amounts of zigzag and armchair boundaries, are not expected to exhibit any polarization dependence. We found that the intensity of the G band of the armchair and zigzag edges has a strong polarization dependence, that is 90º out of phase with respect to each other, as demonstrated in **Figure 14b**. Furthermore, the G band shows no polarization dependence far from the edges, as shown by the black circles in Figure 1b, obtained at the center of the flake. Similar non-polarized data were obtained at numerous different points away from the edges and across the entire flake. Previous experiments on the G band found a variation in amplitude when scanning across a flake at various interior points [16], which is related to Kohn anomalies and an underlying non-uniform strain or deformation potential [17]. Consequently, the lack of polarization dependence at interior points is indicative that the observed phenomenon in our experiments arises from the different allowed and forbidden phonon modes at the edges of the flakes and not from strain-related effects. The presence (absence) of the D band is strongly correlated to 30º multiplicity of the edges as discussed above. This effect originates from the fact that only the longitudinal (transverse) optical phonon mode is a Raman active mode near the armchair (zigzag) edge. Since the physical

mechanism that gives rise to the G band originates from scattering of a doubly degenerate iTO and an LO phonon at the zone boundary, the G band should be better suited for mapping edge states with mixed chirality.

To this end we recorded the polarization contrast of the G band for 3 different edges, as shown in Figure 1c. We found strong correlation of the relative intensity change with the multiplicity of those edges. In contrast, the intensity of the D band showed little sensitivity on the incident photon polarization. More precisely, the particular edge which is 90º to the dominant zigzag edge has the highest (50 %) polarization contrast (purple squares in Fig.1c) while edges with 78º and 72º tilt angle display a polarization contrast of 26% (green dots) and 10% (red triangles), respectively. It should be noted that, in all cases, the polarization dependence of the G-band tends to a minimum value, but never vanishes, suggesting that although the edge is comprised of mostly armchair constituents, it is not atomically clean within the detection area. This verifies prior experimental results [34], which show that atomically smooth edges are very rarely obtained using micromechanical exfoliation. As a result, for mixed-state edges we observe that the G band polarization contrast reflects the fractional composition of armchair and zigzag edges and provides thus information about the purity of the edge, which serves as a convenient process monitor to characterize the degree of edge state purity in patterned graphene.

2.10. Graphene Antidot Superlattices

To elucidate the role of the localized edge state density and its influence on the electronic and optical properties, we introduced a controlled amount of edges by nanopatterning of graphene. Various antidot superlattices were etched onto the exfoliated flakes using electron beam lithography, following an initial Raman characterization to identify the number of layers. **Figure 15a** shows an antidote superlattice and illustrates the filling fractions $F = \phi/s$ of antidots, where ϕ is the antidote diameter and s is the dot separation. In accordance with previous experimental results [18,19], the corresponding Raman spectra display an energetic shift and linewidth narrowing of the G-band with increasing filling fraction. The observed stiffening of the G band from initial 16.7 cm^{-1} in unpatterned graphene to 6.6 cm^{-1} at a filling fractions of two can be understood in terms of the Landau damping of the phonon mode, while the energetic shift arises from a renormalization of the phonon energy [18,20]. Furthermore, we observed that the energetic shift of the G-band is positively correlated with the shift of the G'-band, which is indicative of an effective p-doping of the underlying graphene layer [21,22]. In contrast, a negative correlation in the energetic shifts of the G and G' bands would imply n-doping. In order to correlate shift and stiffening of the G-band in antidot superlattices to an underlying carrier density, we fabricated electrically contacted devices without an antidot lattice, as shown

schematically in **Figure 15b**. Using the electrical field effect of the back gate, the sheet carrier density Δn_s was modulated and the stiffening and energetic shift of the G-band in the unpatterned samples was used to estimate the edge state density in the antidot superlattice. From these data the amount of p-doping in the antidot samples was determined to reach up to $4 \cdot 10^{12}$ cm^{-2} at a filling fraction of two, and was not found to depend on the number of graphene layers. The large amount of effective p-doping is rather remarkable since neither extrinsic dopants, nor an external gate potential were applied to the antidot samples.
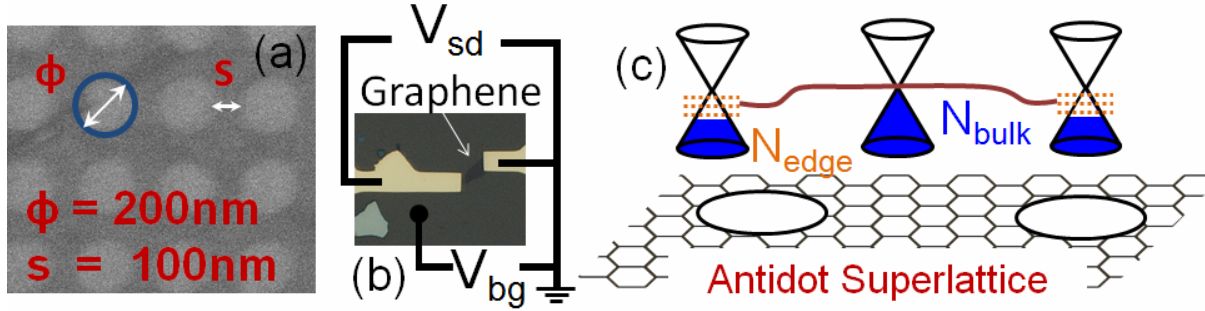

Figure 15 a) Scanning electron microscope (SEM) image of a graphene antidot superlattice fabricated by electron beam lithography. b) SEM of an unpatterned 2 micron long stripe of graphene with the corresponding contacting scheme to study optical emission and Raman signals under applied source-drain and back-gate bias. c) Schematic explanation Fermi-level pinning which occurs at the periphery were the localized edge states Ne$_{dge}$ are located together with a sketch of the resulting band bending.

The remarkable amount of free carriers in the presence of an antidote lattice might originate from an effective electrical field created by the presence of localized edge states. To further investigate the microscopic origin of the observed p-doping we fabricated graphene-dye hybrids. The idea is that the fluorescence and Raman emission of the attached dye molecules can act as an optical monitor for the underlying changes in carrier dynamics and/or the electrical field profile in the nanopatterned graphene flakes. Both, antidot flakes and electrically contacted devices were soaked in a 15 nanomol solution of Rhodamine 6G (R6G). In these experiments, the R6G Raman peaks, the R6G fluorescence, and the Raman signal from graphene were monitored as a function of the antidot filling fraction F as well as different backgate and source-drain biases on the unpatterned flakes. Our results indicate that the R6G fluorescence emission around 577 nm is moderately quenched on the unpatterned graphene substrate as compared to the fluorescence on the bare SiO$_2$ wafer. Remarkably, the fluorescence is quenched even more strongly in the region where the antidot superlattices are located. It was found that the amount of R6G fluorescence quenching increases with increasing filling fraction of the antidots. When the relative intensity of the broad fluorescence signal was normalized to the intensity of R6G fluorescence on the bare SiO$_2$ substrate a quenching up to a factor of five for the largest realized filling fraction was

estimated. In contrast to the quenching fluorescence signal, the intensity of the Raman signals from both R6G and graphene were found to increase six-fold with increasing filling fraction, i.e. increasing density of edge states N_{edge}. The fluorescence quenching may be understood as follows. The incident laser light creates electron-hole pairs in the R6G dye. In the absence of the graphene substrate the electron hole pairs in the dye molecules recombine radiatively, thereby giving rise to the fluorescence signal on the bare SiO_2 wafer. It was previously shown that placing quantum dots on top of graphene results in an energy transfer from the dots into the underlying graphene layer [23], resulting in a suppression of blinking from the quantum dots. A similar effect is expected to occur for the R6G molecules on graphene, where the radiative recombination of the excitons in the R6G molecule is suppressed. In our experiments, additional quenching of the fluorescence signal in the antidot regions was observed as described above. The additional quenching can thus be understood to arise from the extra states at the edges N_{edge}, that effectively prevents radiative recombination of the electron-hole pairs, and therefore quench the fluorescence signal. The amount of quenching observed in our experiments is rather remarkable since increasing the antidot filling fraction decreases graphene's surface area and introduces larger areas of SiO_2 into the excitation volume on which the fluorescence is not quenched.

In order to further elucidate the mechanism for fluorescence quenching and the nature of N_{edge} we fabricated electrically contacted and back-gated graphene flakes, which did not contain an antidote superlattice, as shown in Figure 2b. Varying the backgate voltage, effectively moves the Fermi level in the device thereby affording the possibility of in-situ electron and hole doping of the graphene flake according to $\Delta n_s = C_g (V_g - V_{Dirac})/e$, where C_g is the gate capacitance, V_g is the applied gate voltage, V_{Dirac} is the location of the Dirac point, and e is the electron charge [54-56]. Modulating the Fermi level with the backgate creates a free sheet carrier density in the underlying graphene layer. It was found that the intensities of both the Raman peaks as well as the fluorescence signal can be either quenched or enhanced by the applied gate bias, and directly follow the free carrier density in the device. It is evident that the enhancement of the Raman peaks achieved in antidot devices occurs at comparable concentrations of N_{edge} and sheet carrier densities n_s in unpatterned samples. Unlike the Raman peaks, the R6G fluorescence is strongly quenched in the nanopatterned samples, whereas it is enhanced in the electrically gated samples. The contrasting behavior of the fluorescence signal is strongly indicative of the different nature of the carriers in the antidot superlattice as compared to unpatterned graphene, and can be used to establish a microscopic mechanism for the observed fluorescence quenching and p-doping in the nanostructured samples.

Two possible mechanisms could be responsible for fluorescence quenching: charge transfer from R6G into the trap states that are created by the additional edge state density or electrical field

dissociation of the radiative R6G exciton, which leads to a strong decrease in the exciton recombination rate due to the reduced electron-hole wavefunction overlap in an electric field. Although charge transfer into trap states could account for the decrease of the fluorescence intensity, it cannot explain the observed stiffening and the energetic shift of the G-band phonon in graphene, both of which require an electric field effect. In contrast, the field dissociation mechanism explains both phenomena, as well as the absence of fluorescence quenching in unpatterned graphene under back-gate sweeping. Since the edge states create spatially localized carriers, which are immobile, they would not cause the G-band stiffening. However, their presence effectively pins the Fermi level at the edges, thereby bending the band structure throughout the entire antidot superlattice, since no localized states exist in graphene's basal plane and the Fermi level must remain continuous, as shown schematically in Figure 2c. This band bending creates an effective potential, i.e. a built-in lateral electrical field, that accounts for the dissociation of the R6G excitons, resulting in the observed fluorescence quenching. In contrast, the vertical back-gate field of the unpatterned graphene device does not lead to band bending, while the created free carrier density can effectively feed the carrier capture into the R6G molecules, causing the observed fluorescence enhancement. The Raman signals are enhanced by the electrical field mechanism providing free carriers in both cases. Finally, the effect of the built-in electrical field may be estimated to first order from the amount of p-doping that it introduces. In graphene, doping is commensurate with the movement of the Fermi level into the conduction or valence bands by the electrical field. The band offset ΔE_F as a function of doping concentration n is given by $\Delta E = \eta v_F k_F$. where η is the Planck's constant, v_F is the Fermi velocity, and k_F is the Fermi wave vector, which in graphene is given by $k_F = \sqrt{\pi n}$. The antidot lattices used in our experiments yielded doping concentrations on the order of $0.5\text{-}4\cdot10^{12}$ cm^{-2}, which correspond to band offsets of $\Delta E_F = 90\text{-}260$ meV. The Fermi level pinning at the localized carrier density in the antidot superlattice is similar to Fermi level pinning of a Schottky barrier at an graphene-metal interface that is used to separate photogenerated carriers in optoelectronic devices based, for example, on carbon nanotubes. In our case, however, no metal was deposited onto graphene and the pinning occurs at the localized edge states that are a direct consequence of the antidot superlattice.

3. SUMMARY

We have successfully fabricated in-plane grown arrays of purely semiconducting SWNTs by utilizing tailored nanoscale catalyst patterns, an optimized low-pressure CVD growth process, and an electrical burn-in technique. For segmentation of bridged CNTs into QDs, both AFM-based local oxidation and a top-contacting approach have been incorporated. We have

characterized 200 nm short SWNT segments and successfully observed conductance oscillations in the Coulomb blockade regime up to 200 K, demonstrating SET operation of our devices. We are in the process of further studying and improving the SET device performance by further reducing hysteresis and by creating SWNT-QD devices with much shorter segment length, such that the SET devices can operate at room temperature. For graphene research, the conductivity oscillations were observed with aperiodic spacing to only one side of the tunneling current in a dual-gated graphene field effect transistor with an n-p-n type potential barrier. This observation is of importance for future development and modeling of graphene based nanoelectronic devices. Further, we have investigated the influence of graphene's chiral edges on the electronic and optical properties. It was found that the Raman G band (1580 cm^{-1}) in bilayer graphene is particularly sensitive to the laser polarization with its intensity dependence being out of phase by 90º in the armchair and zigzag case. Moreover, we found that the G band polarization contrast reflects the fractional composition of armchair and zigzag edges, providing a convenient optical monitor to characterize the degree of edge state purity in graphene. To elucidate the role of the localized edge state density we introduced a controlled amount of edges by nanopatterning graphene into antidot superlattices. The nanopatterning was found to result in an effective p-type doping which increases with larger filling fractions, as evident from the corresponding Raman signatures. Further, we showed that, after depositing dye molecules on these flakes, the corresponding fluorescence signal is strongly quenched with increasing antidot filling fraction, while the Raman signal is enhanced. These results are indicative to a microscopic mechanism in which the Fermi level becomes pinned at the antidot periphery giving rise to a built-in electric field, which accounts for the fluorescence quenching and the observed p-type doping in nanopatterned graphene. These findings make antidot superlattices of great interest for carbon-based optoelectronics and might be particularly useful for light-harvesting applications such as photodetectors and solar cells requiring efficient field separation of electron-hole pairs.

REFERENCES

1. N. Ai, O. Sul, M. Begliarbekov, Q. Song., K. Kumar, D. S. Choi, E. H. Yang, S. Strauf, "Transconductance and Coulomb Blockade Properties of In-plane Grown Carbon Nanotube Field Effect Transistors," *Nanoscience and Nanotechnology Letters*, 2 (2), 73-78, 2010
2. W. Kim, *et al, Nano Letters*, 3, 193-198, (2003).
3. M. Begliarbekov, O. Sul, N. Ai, E.H. Yang, S. Strauf, "Aperiodic conductivity oscillations in quasi-ballistic graphene heterojunctions", *Appl. Phys. Lett.* 97, (2010).
4. O.Sul, M. Begliarbekov, C. Tsai, Y. Kim, V. Patil, S. Strauf, and E. H. Yang, "CVD-assisted Atomically Precision Cutting of Graphene Strips with Specific Boundaries", *Graphene Week*, Maryland, MD, (2010).

5. M. Evaldsson, I. V. Zozoulenko, H. Xu, & T. Heinzel, "Edge-disorder-induced Anderson localization and conduction gap in graphene nanoribbons", *Phys. Rev. B* 78, 161407 (2008).

6. L. Ci, Z. Xu, L.Wang, W. Gao, F. Ding, et al.,"Controlled nanocutting of graphene", *Nano Research* 1 (2), 116-122 (2008).

7. Y. Son, L. M. Cohen, and S. G. Louie, "Energy Gaps in Graphene Nanoribbons", *Phys. Rev. Lett*. 97, 216803 (2006).

8. M. Begliarbekov, O. Sul, S. Kalliakos, E. H. Yang, S. Strauf, "Determination of Edge Purity in Bilayer Graphene Using Raman Spectroscopy", *Appl. Phys. Lett.* 97, 031908 (2010).

9. D. Graf, F. Molitor, K. Ensslin, C. Stampfer, A. Jungen, C. Hierold, and L. Wirtz, Spatially Resolved Raman Spectroscopy of Single- and Few-Layer Graphene, *Nano Lett*. 7, 238-242, (2007).

10. A. C. Ferrari, J. C. Meyer, V. Scardaci, C. Casiraghi, M. Lazzeri, F. Mauri, S. Piscanec, D. Jiang, K. S. Novoselov, S. Roth, and A. K. Geim, "Raman Spectrum of Graphene and Graphene Layers", *Phys. Rev. Lett*. 97, 187401 (2006).

11. L. M. Malard, M. A. Pimenta, G. Dresselhaus, and M. S. Dresselhaus, "Raman spectroscopy in graphene", *Phys. Rep*., 47, 51-87 (2009).

12. D. M. Basko, S. Piscanec, and A. C. Ferrari, "Electron-electron interactions and doping dependence of the two-phonon Raman intensity in graphene", *Phys. Rev. B* 80, 165413 (2009).

13. D. L. Mafra, L. M. Malard, S. K. Doorn, H. Htoon, J. Nilsson, A.H. Castro Neto, and M. A. Pimenta., "Observation of the Kohn anomaly near the K point of bilayer graphene", *Phys. Rev. B,* 80, 241414(R) (2009).

14. A. C. Ferrari and J. Robertson, "Interpretation of Raman spectra of disordered and amorphous carbon", *Phys. Rev. B*, 61, 14095, (2000).

15. L. G. Cancado, M. A. Pimenta, B. R. A. Neves, M. S. S. Dantas, and A. Jorio, "Influence of the Atomic Structure on the Raman Spectra of Graphite Edges", *Phys. Rev. Lett*., 93, 247401, (2004) .

16. J. Yan, E. A. Henriksen, P. Kim, and A. Pinczuk, "Observation of Anomalous Phonon Softening in Bilayer Graphene", *Phys. Rev. Lett*., 101, 136804, (2008).

17. M. Huang, H. Yan, C. Chen, D. Song, T. F. Heinz, and J. Hone, "Phonon softening and crystallographic orientation of strained graphene studied by Raman spectroscopy", *Proc. Nat. Acad. Sci*., 106, 7304-7308, (2009).

18. J. Yan, Y. Zhang, P. Kim, A. Pinczuk, "Electric Field Effect Tuning of Electron-Phonon Coupling in Graphene", *Phys. Rev. Lett.*, 98, pp. 166802, (2007).

19. S. Pisana,M. Lazzeri, C. Casiraghi, K.S. Novoselov, A.K. Geim, A.C. Ferrari,F. Mauri, "Breakdown of the adiabatic Born–Oppenheimer approximation in graphene", *Nature Materials*, 6, 198 – 20, (2007).
20. A.C. Ferrari, "Raman spectroscopy of graphene and graphite: Disorder, electron–phonon coupling, doping and nonadiabatic effects", *Sol. Stat. Comm*., 143, 47–57, (2007).
21. A. Das, S. Pisana, B. Chakraborty,S. Piscanec, S.K. Saha, U.V. Waghmare, K.S. Novoselov, H.R. Krishnamurthy, A.K. Geim, A.C. Ferrari, and A.K. Sood, "Monitoring dopants by Raman scattering in an electrochemically top-gated graphene transistor", *Nature Nanotechnology*, 3, 210 – 215 (2008).
22. C. Stampfer, F. Molitor, D. Graf, K. Ensslin, A. Jungen, C. Hierold, and L. Wirtz, "Raman imaging of doping domains in graphene on SiO_2" , *Appl. Phys. Lett*., 91, 41907, (2007).
23. Z. Chen, S. Berciaud, C. Nuckolls, T.F. Heinz, L.E. Brus, "Energy Transfer from Individual Semiconductor Nanocrystals to Graphene", *ACS Nano*, 4, 2964-2968, (2010).

Personnel:

Faculty:
PI: Professor Eui-Hyeok Yang (Stevens, ME)
Co-PIs: Professors Stefan Strauf (Stevens, Physics), Frank Fisher (Stevens, ME) and Daniel Choi (U. Idaho, Materials)

Post-docs: Dr. Onejae Sul

Graduate Students: Anderson Tsai, Kitu Kumar, Milan Begliarbekov, Nan Ai, Qiang Song, Will Walden-Newman

Publications/Accepted or In Print (partially or fully supported by this project):

Journals

1. M. Belgiarbekov, O. Sul, J. Santanello, N. Ai, X. Zhang, E.H. Yang, and S. Strauf, "Localized States and Resultant Band Bending in Graphene Antidot Superlattices," *Nano Letters,* **11**, 1254–1258 (2011).
2. N. Ai, W. Walden-Newman, Q. Song, S. Kalliakos, and S., "Suppression of blinking and enhanced exciton emission from individual carbon nanotubes" *ACS Nano* **5**, 264-2770 (2011).
3. K. Kumar, O. Sul, S. Strauf, F. Fisher, D. S. Choi, M. G. Prasad, and E. H. Yang, "A Study on Nanoscale Carbon Nanotube Local Oxidation Lithography using an Atomic Force Microscope," *IEEE Trans. Nanotechnology (TNANO), in print 2011*
4. M. Belgiarbekov, O. Sul, N. Ai, E.H. Yang, and S. Strauf, "Aperiodic Conductivity Oscillations in Quasi-ballistic Graphene Heterojunctions," *Applied Physics Letters,* **97**, 122106, 2010

5. K. Kumar, S. Strauf, and E.H. Yang, "A Study on Graphite Local Oxidation Lithography Using an Atomic Force Microscope," *Nanoscience and Nanotechnology Letters*, **2** (2), 185–188, 2010

6. D. S. Choi, J.-R. Park, S. Lee, T. Hahn, N. Presser, M. Leung, G. Stupian, E. H. Yang, and F Khalid, "Microcapacitors based on Electrochemically Grown Vertical Arrays of Gold Nanowire as Electrodes," *Thin Solid Films,* **518** (17), 5007-5009, 2010.

7. N. Ai, O. Sul, M. Begliarbekov, Q. Song., K. Kumar, D. S. Choi, E. H. Yang, S. Strauf, "Transconductance and Coulomb Blockade Properties of In-plane Grown Carbon Nanotube Field Effect Transistors," *Nanoscience and Nanotechnology Letters*, **2** (2), 73-78, 2010

8. Z. Zhang, N. Dahal, K. Xu, and D. Choi, E. H. Yang and J. R. Park, "Electrochemical Characterization of Tin Quantum Dots Grown on a Carbon Nanotube Mat as Anodes for Battery Applications," *Nanoscience and Nanotechnology Letters*, **2** (2), 86-88, 2010

9. M. Belgiarbekov, O. Sul, S. Kalliakos, E. H. Yang, and S. Strauf, "Determination of Edge Purity in Bilayer Graphene using μ-Raman Spectroscopy," *Applied Physics Letters,* **97**, 031908, 2010

10. O. Sul, S. Jang and E. H. Yang, "Step-Edge Calibration of Torsional Sensitivity for Lateral Force Microscopy," *Measurement Science and Technology*, **10**, 115104, 2009

11. S. W. Lee, S. S. Lee, and E. H. Yang, "A Study on Field Emission Characteristics of Planar Graphene Sheets Obtained from a Highly Oriented Pyrolyzed Graphite Block*," Nanoscale Research Letters,* **4** (10), 1218-1221, 2009.

12. D. S. Choi, V. Fucsko, E. H. Yang., J.-R. Park, F. Khalid and Y.-K. Kim, "Vertical Arrays of Copper Nanotube Grown on Silicon Substrate by CMOS Compatible Electrochemical Process for IC Packaging Applications," *Journal of Microelectronics and Electronic Packaging,* **6** (3), 154-157, 2009

13. O. Sul ad E. H. Yang, "A Multi-Walled Carbon Nanotube-Aluminum Bimorph Nanoactuator," *Nanotechnology* **20**, 095502, 2009.

14. J. Yang, H. J. Yoon, E. H. Yang, S. S. Yang, "A nickel nanowire diluter operating through the principle of the dielectrophoretic attraction force," *Transactions of the Korean Institute of Electrical Engineers* **59** (2), 385-389 (2010)

Conference Proceedings

1. O.Sul, M. Belgiarbekov, J. Santanello, N. Ai, X. Zhang, E.H. Yang, and S. Strauf, "Fluorescene Quenching by Local Electronic States around Graphene Antidot Superlattices" *Nano Korea Symposium*, Kintex, Seoul, Republic of Korea, August 24~26. 2011

2. S. Strauf and E. H. Yang, "Graphene Optoelectronics based on Antidot Superlattices," *Invited Paper*, *SPIE Defense and Security Symposium, Micro- and Nanotechnology Sensors, Systems, and Applications, Conference*, Orlando, FL, April 2011.

3. K. Kumar and E. H. Yang, "Nanoscale Graphene Lithography Using an Atomic Force Microscope," *TechConnect World Conference and Expo 2010*, Anaheim, California, June 21-25, 2010

4. E. H. Yang, "Engineered Nanowires, Carbon Nanotubes and Graphene for Sensors, Actuators and Electronics," *Invited Paper*, *SPIE MEMS-MOEMS, San Francisco, Jan. 2010*.

5. N. Ai, Y. T. Tsai, E. H Yang, D. S. Choi and S. Strauf, "Electro-optical Characterization of Individual Multiwall Carbon Nanotubes," *SPIE Defense and Security Symposium, Micro- and Nanotechnology Sensors, Systems, and Applications, Conference 7318 - Proceedings of SPIE Volume 7318*, Orlando, FL, April 2009.

6. S. Jang, S. Manoochehri and E. H. Yang, "Fabrication of Vertically Standing Metal Nanowire Arrays on Silicon and Glass Substrates using Polycarbonate Membrane," *Defense and Security Symposium, Micro- and Nanotechnology Sensors, Systems, and Applications, Conference 7318 - Proceedings of SPIE Volume 7318*, Orlando, FL, April 2008.

7. O. Sul and E. H. Yang, "Development of Carbon Nanotube-Based Nanoactuator for Nano-Conveyer System", *ASME International Mechanical Engineering Congress and Exposition*, Boston, MA, Nov

2008
8. H. J. Yoon, J. H. Yang, S. S. Yang, and E. H. Yang, "Microfabricated Nanowire Sorter for Nanowire Assembly", *ASME International Mechanical Engineering Congress and Exposition*, Boston, MA, Nov. 2008.
9. D. S. Choi, V. Fucsko and E. H. Yang, "Copper Nanotubes for Packaging Applications," *IEEE Aerospace Conference*, Big Sky, Montana, USA, April 2008.

Conference Presentations

1. K. Kumar, O. Sul, Y. T. Tsai, S. Strauf, F. Fisher, D. S. Choi and E. H. Yang, "Nanoscale Graphene Lithography Using an Atomic Force Microscope" *Graphene Week*, Maryland, MD, April, 2010.
2. O. Sul, M. Begliarbekov, C. Tsai, Y. Kim, V. Patel, S. Strauf, and E. H. Yang, "CVD- assisted Atomically Precision Cutting of Graphene Strips with Specific Boundaries," *Graphene Week*, Maryland, MD, April, 2010.
3. M. Begliarbekov, O. Sul, C. Tsai, N. Ai, E. H. Yang and Stefan Strauf, "Observation of Klein Tunneling in Top-Gated Graphene Transistors," *Graphene Week*, Maryland, MD, April, 2010
4. K. Kumar, O. Sul, Y. T. Tsai, S. Strauf, F. Fisher, D. S. Choi and E. H. Yang, "Nanoscale Graphene and Carbon Nanotube Lithography using an Atomic Force Microscope" *ASME International Mechanical Engineering Congress and Exposition*, Lake Buena Vista, FL, Nov 2009
5. M. Belgiarbekov, O. Sul, N. Ai, C. Tsai, J. Hereaux, E. H. Yang, and S. Strauf, "Characterization of Graphitic thin films and top-gated Klein transistors", NYAS Gotham-Metro, *Condensed Matter meeting*, 2010.
6. M. Begliarbekov, O. Sul, N. Ai, Q. Song, S. Kalliakos, C. Tsai, K. Kumar, J. Heureaux, E. H. Yang, S. Strauf, Quantum transport in graphitic nanostructures, *GK-12 Conference,* Washington DC, USA, 2010.
7. S. W. Lee, S. S. Lee and E. H. Yang, "Field Emission from Graphene Structures for Vacuum Transistor Applications," *ASME International Mechanical Engineering Congress and Exposition*, Lake Buena Vista, FL, Nov 2009
8. O. Sul, S. Jang and E. H. Yang, "Characterization of Thermomechanical Properties of Polypyrrole Nanowires," *ASME International Mechanical Engineering Congress and Exposition*, Lake Buena Vista, FL, Nov 2009

Interactions/Transitions (partially or fully supported by this project):

1. E. H. Yang, "Engineered Nanomaterials for Nanoelectronics and Microfluidics," Montana State University, Montana, November 2010.
2. E. H. Yang, "Engineered Carbon Nanotube and Graphene for Nanoelectronics and Nanomechatronics," NASA Jet Propulsion Laboratory, California, May 2010.
3. E. H. Yang, "Engineered Carbon Nanotube and Graphene for Nanoelectronics and Nanomechatronics," NASA Goddard Space Flight Center, Maryland, April 2010.
4. E. H. Yang, "Engineered Carbon Nanotube and Graphene for Sensors, Actuators and Nanoelectronics," Louisiana State University, Oct. 2009
5. E. H. Yang, "Engineered Carbon Nanotube and Graphene Materials for Nanoelectronics, Sensors and Actuators," CCNY, Sept. 2009.

Other interactions include the following technical presentations:

New Discoveries, Inventions, or Patent Disclosures:

1. K. Kumar and E. H. Yang, "A High-throughput Local Oxidation Patterning Process," U.S. Patent Filed from Stevens: 12/732,518

Honors/Awards:

1. S. Strauf, "Grapheotonics: Photonics with Carbon Nanotubes and Graphene", Recipient of the "Lange Lecturer" of the Materials Department at UC Santa Barbara, Feb 2011.
2. S. Strauf, Provost Award "In recognition of outstanding achievements in research and scholarship", Jan 2011.